Approximate entropy analysis for nonlinear beam dynamics

Yongjun Li [*] and Robert Rainer
Brookhaven National Laboratory, Upton 11973, New York, USA

(Received 3 July 2023; accepted 2 January 2024; published 11 January 2024)

In this paper, we applied an approximate entropy (ApEn) analysis to nonlinear beam dynamics. Due to the presence of strong nonlinear magnets, the degree of chaos in beam motion gradually increases proportionally with its amplitude. Such chaos can be quantitatively characterized with ApEn of beam turn-by-turn readings. ApEn analysis is a technique used to quantify the amount of regularity and the unpredictability of fluctuations with respect to time-series data. The ApEn, when applied as a chaos indicator, can then be used for nonlinear lattice optimization and analysis. The National Synchrotron Light Source II (NSLS-II) electron storage ring lattice was used as an example of a real-world application of our technique.

DOI: 10.1103/PhysRevAccelBeams.27.011601

I. INTRODUCTION

For circular particle accelerators, the nonlinearity of beam dynamics confines long-term motion stability within a limited region in six-dimensional phase space, namely, the dynamic aperture (DA) [1]. Even within the DA, particle motion may still be chaotic. It is commonly believed that, for a given magnetic lattice, by suppressing the chaos of the system, one can enlarge the DA and local momentum aperture (LMA), thereby enhancing its robustness to errors and imperfections. Various chaos indicators have been adopted to characterize the nonlinearity of beam motion [2], such as the Lyapunov exponent [3–5], frequency map analysis (FMA) [6], forward-reversal integration (FRI) [7–9], data-driven chaos indicator [10], fluctuation of approximate invariant [11], etc. In this paper, we apply approximate entropy (ApEn) to analyze the nonlinear beam dynamics.

The concept of entropy has its origins in classical physics under the second law of thermodynamics. In the context of nonlinear dynamics, information entropy is central in quantifying the degree of uncertainty or information gain. It is widely used to explain complex nonlinear behavior in real-world systems. Among many entropy analyses, the concept of ApEn was initially developed by Pincus [12] to analyze medical data, such as heart functions (rate, impulse, etc.) Applications of the ApEn later spread to many other fields, such as finance [13], nonlinear dynamics [14], etc. It is now widely used as a technique to quantify the amount of irregularity and the unpredictability of fluctuations, particularly for systems with noise components and short time-series data.

Due to the presence of strong nonlinear magnetic fields in circular accelerators, the chaos of beam motion gradually increases with its amplitude. Chaos of a dynamical system is often visualized with the Poincaré map. For beam dynamics, it is seen at the intersection of periodic orbit projected in a certain lower-dimensional subspace, usually a two-dimensional conjugate coordinate-momentum phase space. Experimentally, it can also be observed from turn-by-turn (TBT) data collected by beam position monitors (BPMs) after the beam is excited. ApEn can quantitatively characterize the chaos of the circulating beam from the TBT readings. Based on that, the suitability of the configuration of magnetic lattices can be determined. Therefore, the ApEn as a chaos indicator can be used for nonlinear lattice optimization at the design stage. It can also be used for online beam-based optimization, [15] provided the BPMs TBT resolution is sufficient.

The remainder of this paper is outlined as follows: Sec. II reviews the definition of ApEn and briefly explains its underlying principles. In Sec. III, an ApEn analysis is applied to a Hénon map as a proof of principle. In Sec. IV, as a real-world application, the ApEn observed in the transverse x-y plane is used as a minimization objective to optimize the National Synchrotron Light Source II (NSLS-II) nonlinear lattice. In Sec. V, we implement a detailed ApEn analysis for an elite candidate selected from the previous optimization and can then interpret the physics information that is conveyed by this analysis. A summary is given in Sec. VI.

II. APPROXIMATE ENTROPY

According to Pincus, ApEn is computed with the following steps [12,16]. Fix m as a positive integer and r as a positive real number. Given time-series data $u_1, u_2, \ldots, u_N$, from measurements equally spaced in time,

[*] yli@bnl.gov

Published by the American Physical Society under the terms of the Creative Commons Attribution 4.0 International license. Further distribution of this work must maintain attribution to the author(s) and the published article's title, journal citation, and DOI.

form a sequence of vectors $\vec{x}_1, \vec{x}_2, \ldots, \vec{x}_{N-m+1}$, defined by $\vec{x}_i = [u_i, u_{i+1}, \ldots, u_{i+m-1}]$. Next, define the correlation parameter [17] for each i, $1 \le i \le N - m + 1$,

$$C_i^m(r) = (\text{number of } j \text{ such that } d[\vec{x}_i, \vec{x}_j] \le r)/(N - m + 1), \tag{1}$$

here the distance $d[\vec{x}_i, \vec{x}_j]$ is defined as

$$d[\vec{x}_i, \vec{x}_j] = \max_{k=1,2,\ldots,m}(|u_{i+k+1} - u_{j+k+1}|). \tag{2}$$

The $C_i^m(r)$'s measure, within the tolerance of r, the regularity or frequency of patterns similar to a given pattern of window length m. Next, define

$$\varphi^m(r) = \frac{1}{N - m + 1} \sum_{i=1}^{N-m+1} \ln C_i^m(r), \tag{3}$$

where ln is the natural logarithm. Finally, the parameter

$$\mathrm{ApEn}(m, r) = \lim_{N\to\infty}[\varphi^m(r) - \varphi^{m+1}(r)], \tag{4}$$

is defined as the approximate entropy.

Fundamentally, ApEn measures the conditional probability that nearby pattern runs remain close in the next incremental comparison [16,18]. A positive ApEn usually indicates the presence of chaos [19]. In real-world applications, the length of input time series N cannot be infinite as defined in Eq. (4). A practical value of N is typically between 75 and 5000, depending on the availability of valid data. Based on the calculations that include both theoretical analysis and clinical applications, Pincus concluded that for $m = 1$, 2, and values of a filter r between $0.1\sigma_u$ to $0.25\sigma_u$, σ_u is the standard deviation of the u_i data and can produce good statistical validity [16]. By checking turn-by-turn simulation data for the NSLS-II lattice (as will be discussed in Sec. IV), we found that such configurations are also applicable to its nonlinear beam dynamics.

ApEn can be computed directly based on the above definition. Its required execution time is analogous to the square of the size of the input signal. Fast algorithms, such as [20], were proposed to speed up its computation. In the meantime, well-developed and documented computation packages, such as EntropyHub [21], are also available.

III. APPLICATION OF THE HÉNON MAP

In this section, an ApEn analysis is applied to a well-studied one-dimensional quadratic Hénon map [22] with dissipation,

$$\begin{pmatrix} x \\ p \end{pmatrix}_n = \begin{pmatrix} \cos\mu & \sin\mu \\ -\sin\mu & \cos\mu \end{pmatrix} \begin{pmatrix} x \\ p - \lambda x^2 - \Delta p \end{pmatrix}_{n-1}. \tag{5}$$

From the view of beam dynamics, this discrete map represents a simple lattice structure composed of a thin lens sextupole kick followed by a linear phase space rotation at a phase advance of $\mu = 2\pi\nu$, and the dissipation Δp can represent the synchrotron radiation damping. Here, the normalized sextupole strength is $\lambda = 1$, and the linear tune is chosen to be $\nu = 0.205$, to produce the fifth-order resonance crossing at certain amplitudes. Finding the dynamic aperture of this map is straightforward due to its low computational demand. The ApEn analysis, however, was applied here to demonstrate its ability to identify the system's chaos and nonlinear resonances as a proof-of-principle.

The map is iterated for 512 runs, then the ApEns of x coordinates are computed for each initial condition in the phase space x-p. To mimic the measurement noise, a random 0.1% error Δx was added to each x reading, Here we chose the parameters $m = 2$, $r = 0.2\sigma_x$, and σ_x is the standard deviation of each time-series dataset, x in computing the ApEn. The chaos measured with its ApEn increases gradually with the initial condition's amplitude $\sqrt{x^2 + p^2}$, except when crossing stable resonances as illustrated in Fig. 1. The contours of FMA analysis are also computed for comparison purposes. A detailed performance comparison among several other chaos indicators, such as FMA, FRI, Lyapunov exponent, etc., was well studied in Ref. [2].

Although the ApEn gradually increases with initial amplitude in Fig. 1, we also observed that it is not monotonic,

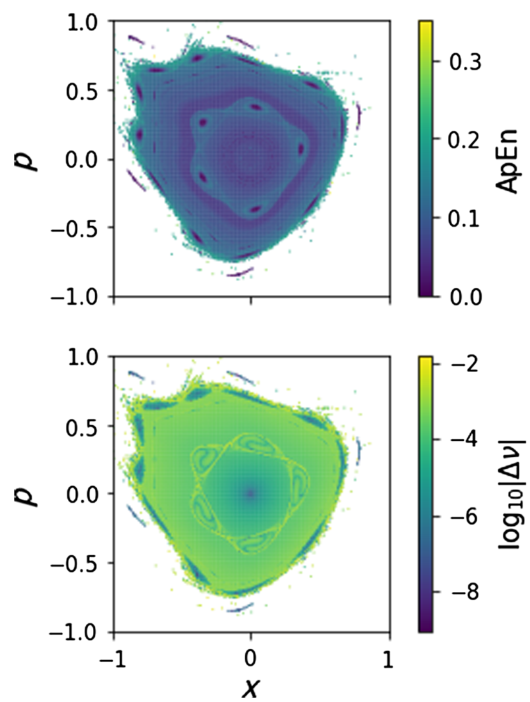

FIG. 1. Comparison of the ApEn (top), FMA (bottom) analyses for a Hénon map with 512 iterative runs. The color maps represent the ApEn and tune diffusion at the locations of their initial conditions. The blank area represents unbounded trajectories.

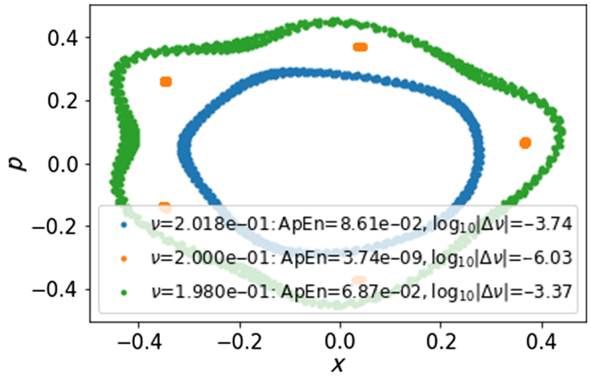

FIG. 2. Trajectories of the Hénon map in the phase space while crossing a fifth-order resonance. Once the tune is sufficiently close to 0.2, and the trajectory can be trapped around the fixed points. The corresponding motion in the time domain almost repeats itself with a periodicity of 5. Therefore, a near-zero ApEn is observed.

particularly, when crossing the fifth-order resonance, low ApEn values were read. Figure 2 shows three trajectories in the x–p Poincére section while crossing the resonance. When the tune is sufficiently close to 0.2, and their trajectories are trapped around five elliptical fixed points (FP), isolated islands are formed and trajectories gradually merge with the FPs. Around those stable FPs, the fundamental tune diffusion is at the order of 10^{-6} with 512 turns data. However, because the dimension of islands is sufficiently small, the time-series data composed of x (or p) almost repeats itself with a periodicity of 5, which yields a near-zero ApEn.

IV. APPLICATION FOR NONLINEAR LATTICE OPTIMIZATION

In this section, we use ApEn as a chaos indicator to optimize the nonlinear lattice for the NSLS-II storage ring. In a linearly stable lattice, the motion of particles seen by a BPM at certain locations can be represented as a periodic time series, oscillating with a fixed frequency of $2\pi\nu$. This ν is known as the linear tune. Nonlinear magnets, such as sextupoles for chromaticity correction, can perturb regular beam motion. Thus, signals seen by the BPM now have fluctuations on top of the regular motion. The ApEn of the TBT BPM readings reflects the likelihood that similar patterns of the TBT readings will not be followed by additional similar readings. Given a nonlinear lattice, if the ApEns of TBT readings are low, the beam motion is less chaotic and vice versa. By minimizing the ApEn of different trajectories through tuning nonlinear "knobs" (i.e., sextupoles), the lattice can be optimized.

First, we need to determine the needed length of TBT data to detect the chaos for a given lattice. Here, we use the current NSLS-II operational lattice for demonstration. From a certain longitudinal observation location (such as the center of the long straight section for injection), multiple initial conditions are uniformly populated within

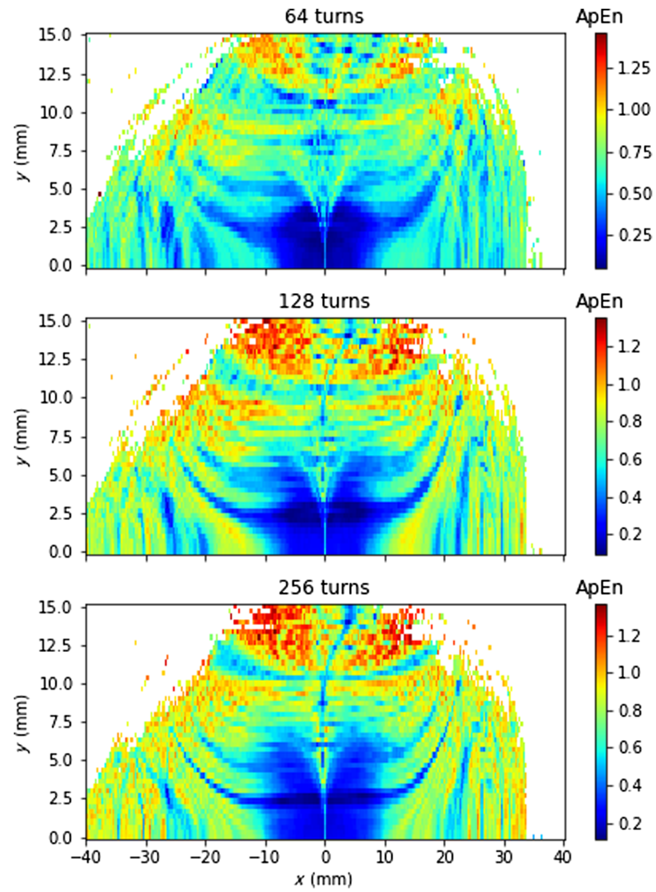

FIG. 3. ApEns computed with 64, 128, and 256-turns TBT data for the NSLS-II operational lattice. Although longer TBT data provide more accurate information on the distribution of chaos, the overall chaos map is already visible even with just the 64 turns data.

a region of interest (ROI) with a transverse dimension $x \in [-40, 40]$ mm, and $y \in [0, 15]$ mm (Fig. 4). Usually, the ROI is chosen to be slightly larger than the desired dynamic aperture. Particle trajectories are simulated with a symplectic integrator [23] implemented in the code ELEGANT [9]. Similar to the FMA analysis [6,24], the ApEn of those TBT data starting with the same initial conditions but different turns (64, 128, and 256) were visualized with contour plots as illustrated in Fig. 3.

From our observation, the ApEn analysis yields visible chaos even from smaller sets of TBT data. This means that even short-term TBT data with this method is capable of driving an optimizer. Therefore, early in the design stage, the low computational cost of this method can efficiently narrow down the search range by ruling out undesirable (i.e., with smaller DA and LMA) candidates. Consequently, longer datasets can provide even more detailed chaos information but would require higher computational time/demand.

In the following DA optimization, 256-turns simulated TBT data were used, which can already clearly identify the

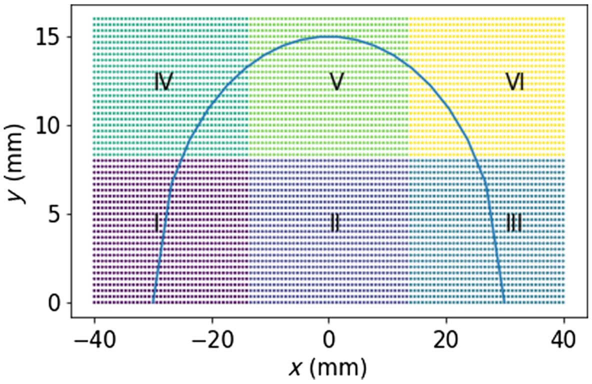

FIG. 4. Dividing the region of interest (ROI) into $2 \times 3 = 6$ zones in the x-y plane at the observation point. In each zone, multiple initial conditions (represented with the same-colored dots) are uniformly populated. The optimization objectives are the averaged ApEns of all initial conditions within each individual zone. The solid elliptical line is the desired DA profile.

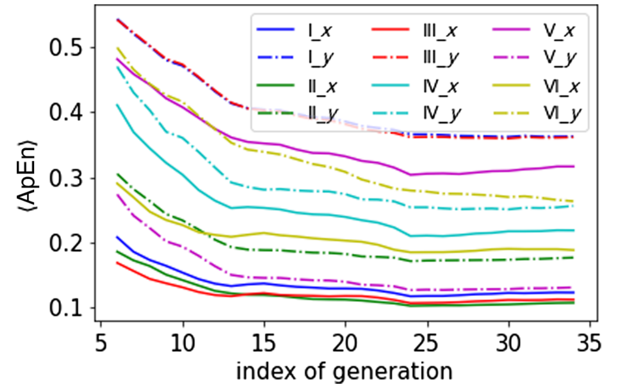

FIG. 5. Convergence of averaged ApEns in the genetic algorithm optimization. Solid lines stand for the horizontal plane, and dashed-dotted ones for the vertical plane. Lines with the same color are from the same zone.

degree of chaos. Conveniently, the needed computational cost for the particle tracking simulation is affordable with commonly available computational resources.

Now, we introduce the detailed optimization implementation using the NSLS-II storage ring as a real-world example. The goal of optimization is minimizing the ApEns for all initial conditions within the ROI. It is neither practical nor necessary to minimize every initial condition simultaneously, therefore, the ROI is divided into several zones as shown in Fig. 4. For each zone, two objectives are the survival after 256 turns of the horizontal and vertical ApEns, averaged over all initial conditions. By tuning the sextupole knobs, we attempted to minimize every zone's ApEns simultaneously to suppress the overall chaos within the whole of the ROI. Many light source rings are composed of multiple identical cells. Therefore, we can even use one cell to optimize its DA for the ideal error-free lattice to quickly narrow down the search range. In the next stage, a full ring lattice, including various imperfections and errors can be used to search for robust solutions within the new, narrower ranges.

In the optimization, ApEns were computed in the horizontal and vertical planes and their values were usually at different scales and needed to be minimized separately. The number of optimization objectives was 2 times the number of zones. The "tuning knobs" in this example were six harmonic sextupole families. These sextupoles do not contribute to the linear chromaticity but can compensate for geometric and chromatic optics aberrations generated by chromaticity correction sextupoles. The range of these sextupoles strengths K_2 is confined within $[-40, 40]$ m^{-3}, limited by their power supply capacities and magnetic saturation.

This multiobjective optimization was accomplished with the widely used genetic algorithm [25–27]. As a small population with 1000 candidates evolved more than 30 generations, a good convergence of the average ApEn was reached (Fig. 5). The DAs of all candidates in the 30th generation were calculated, and from them, some "elite" or desirable configuration candidates were selected. The on-momentum DA profiles of the top 20 elite candidates are illustrated in the top subplot of Fig. 6. It is interesting to note that the distributions of their six tuning knobs (i.e., the sextupole gradients K_2) also converge to some small ranges

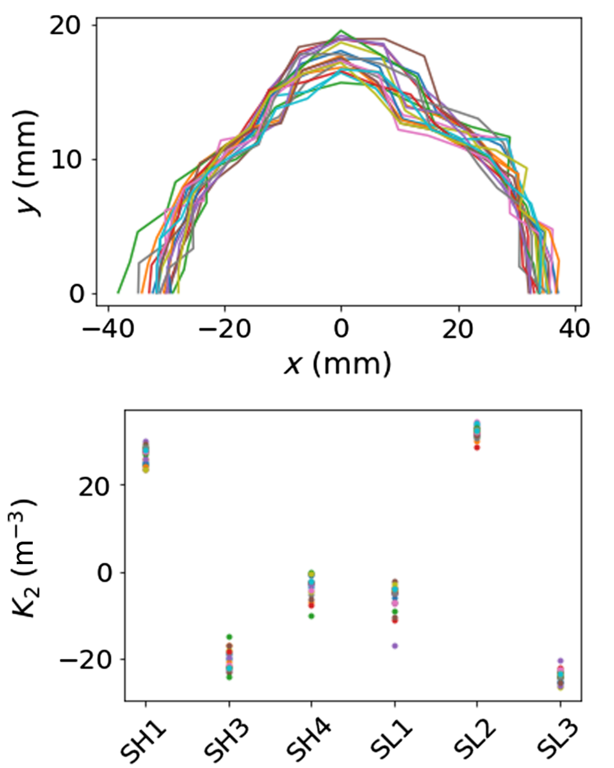

FIG. 6. Top: on-momentum DA profiles for 20 elite candidates selected from the last generation of the genetic algorithm optimization. Bottom: distribution of six sextupole knob configurations of these elite candidates. They converge to some narrow ranges as well.

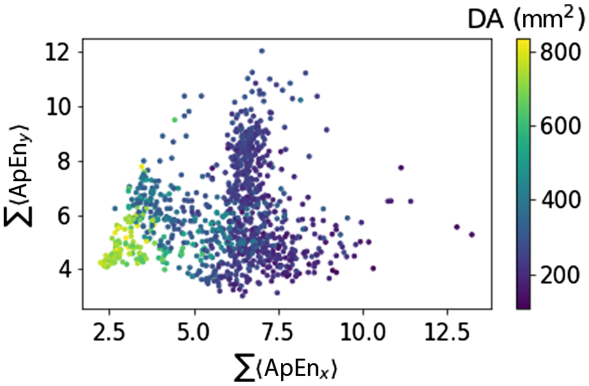

FIG. 7. Correlation between ApEn and DA area. The horizontal and vertical axes are the sums of six zone's averaged ApEns. Each dot represents one candidate in the 30th generation of the genetic algorithm optimization, colored with its area of on-momentum DA. The correlation indicates that having small ApEns in both horizontal and vertical planes plays a role in enlarging the NSLS-II ring's DA.

as shown in the bottom subplot. The correlation between the average ApEns and the area of DAs is illustrated in Fig. 7, which indicates that suppressing the ApEns in both the horizontal and vertical planes plays a role in enlarging the DA.

In designing a nonlinear lattice, the DA and local momentum aperture (LMA) must simultaneously be considered to satisfy the requirements on injection efficiency and beam lifetime [28]. The same strategy as Ref. [8] was used to include some off-momentum DAs as optimization objectives. In this example, on $\delta = \pm 2.5\%$ off-momentum planes, ApEns are added as the objectives, which are evaluated in the same way as Fig. 4. Considering off-momentum DAs are usually smaller than the on-momentum configurations, slightly narrower ROIs were used. The on- and off-momentum ($\delta = \pm 2.5\%$) DAs for a selected elite candidate are illustrated in Fig. 8, which are sufficient to achieve high-efficiency

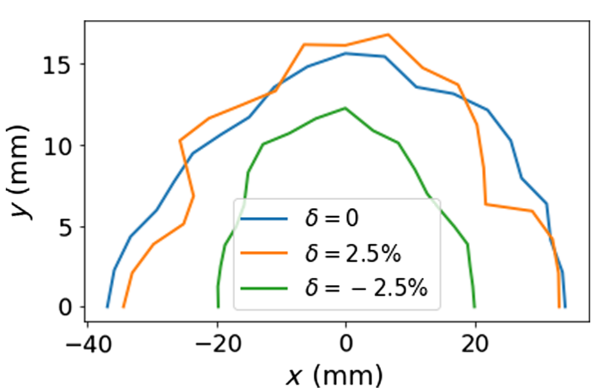

FIG. 8. On- and off-momentum DAs for a selected elite candidate.

injections and 3 h Touschek beam lifetime [29] compared with our current operational lattice.

V. INFORMATION LEARNED FROM ApEn

Like FMA, ApEn can also provide detailed chaos information for a given nonlinear lattice, such as the strength and location of resonances and robustness to errors. Below, we use an elite candidate (the same as shown in Fig. 8) as an example for implementing a detailed ApEn analysis. To achieve a more accurate result, for each initial condition, a $N = 1024$ long TBT dataset was obtained with the code ELEGANT. In the meantime, high density initial conditions were populated to produce a high-resolution DA profile to identify resonance lines. As previously observed in Fig. 5, the horizontal and vertical ApEns are at different scales. Therefore, three ApEn profiles are provided in Fig. 9: two separated ApEn maps observed solely in either the horizontal or vertical plane and one weighted map obtained by adding them after normalizing with their maxima,

$$\mathrm{ApEn}_{x,y} = \frac{\mathrm{ApEn}_x}{\max\ \mathrm{ApEn}_x} + \frac{\mathrm{ApEn}_y}{\max\ \mathrm{ApEn}_y}, \tag{6}$$

where max $\mathrm{ApEn}_{x,y}$ are the maxima in each planes, respectively.

In the horizontal ApEn_x map, besides visible resonances around $x = \pm 20$ mm, strong chaos also appears in the vicinity of the y axis ($x = 0$), particularly when

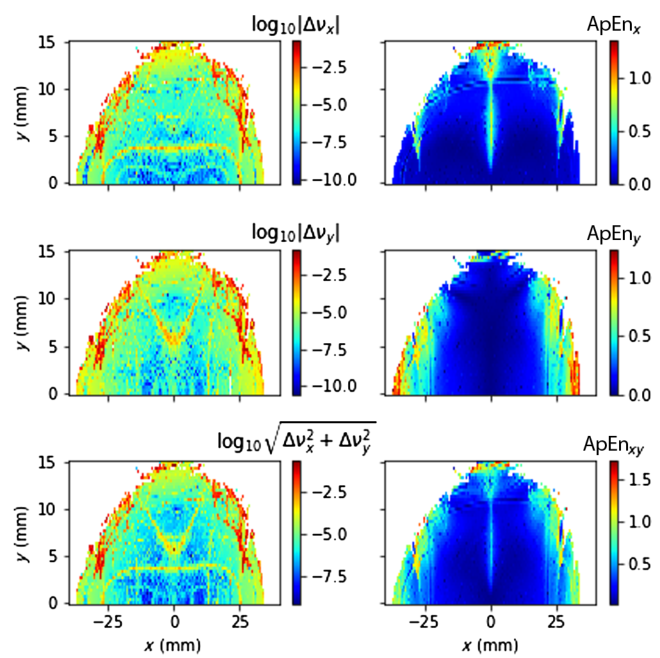

FIG. 9. FMA and ApEn analyses for a selected elite candidate. Left column: tune diffusion maps of FMA observed in the horizontal, vertical, and then both planes. Right column: ApEn maps observed in the horizontal, vertical, and then both planes.

$y \geq 10$ mm. While in the vertical plane, strong chaos shows up when $x \geq |20|$ mm. Based on this observation, we can conclude that a strong nonlinear coupling must exist between two transverse planes. Such coupling drives the vertical motion to be chaotic at large horizontal amplitudes and vice versa. In the vicinity of y axis, small amplitude horizontal TBT data are influenced by the coupling from the vertical plane, thus its signal-to-noise ratio is low, which results in visual chaos there. A larger concern is that such coupling could cause the horizontal DA to reduce significantly in the presence of vertical physical apertures and errors. We use the ApEn_y (see Fig. 9, middle-right subplot) to further illustrate this. When a particle's horizontal amplitude exceeds 20 mm, although the horizontal motion remains regular (shown with "cold" colors in the top-right subplot), its vertical motion becomes significantly chaotic and has large fluctuations, as observed by their TBT data. The particles can still survive in an open space, however, once small vertical physical apertures and/or errors are introduced, they can be lost (i.e., decreased horizontal DA). Such coupling issues are often seen in light source rings, in which in-vacuum undulators (IVU) usually have vertical apertures of a few millimeters and cause a significant reduction of the DA in the horizontal plane. Note that most light source rings require a sufficiently large horizontal DA for injection.

As illustrated in Fig. 10, after a ± 2.5 mm vertical aperture is introduced and the intrinsic NSLS-II magnet systematic multipole errors are accounted for, the horizontal DA is reduced to the area with low ApEn_y. If the area of DA in free space is used as the only objective of optimization, some candidates might be unrealistically estimated. Previously, such difficulty has been overcome by including physical apertures and errors in the tracking simulation and optimization [28], but it greatly slows down the speed of optimization. One of the benefits of using ApEn as the chaos indicator is that, even with error-free magnet models, the robustness of the lattice to errors and physical apertures is made more transparent to a certain extent. Therefore, ApEn is particularly useful in the early stage of lattice optimization in narrowing down the search range for robust solutions, even while lacking information on magnet errors.

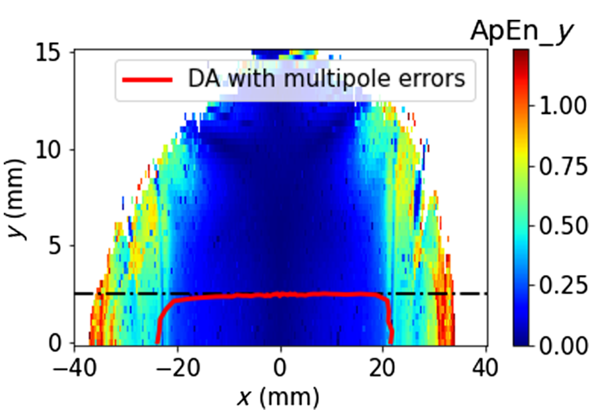

FIG. 10. Reduction of DA when a vertical physical aperture (dash-dot line) and multipole errors are introduced. The horizontal aperture is decreased in the region where the vertical ApEn is high. The DA with imperfections (red solid line) confirms that having a low ApEn is essential in obtaining robust solutions.

The standard FMA analyses are also illustrated in the left column of Fig. 9, for comparison. Three tune diffusion maps (in the horizontal, vertical, and both planes, respectively) gradually increase with their initial amplitudes, but there is no obvious "jump" between the regular and chaotic regime as shown in the subplot of ApEn_y profile. However, FMA does provide a clearer view of the location of resonances.

VI. SUMMARY

In this paper, the ApEn was applied to analyze the chaos of nonlinear beam dynamics. With simulated TBT data, nonlinear lattice configurations can be optimized by minimizing their ApEns. One of the advantages of using the ApEn method is its low computational demand. The ApEn method can be designed to work for small data samples. Therefore, it can be particularly useful in the early stages of nonlinear lattice design when a huge number of lattice configurations need to be screened and evaluated quickly. It can also potentially be applied to online optimizations when the BPM system has the required TBT resolution.

It is important to note that some limitations also exist in the ApEn analysis [18]. The algorithm counts each sequence as matching itself to avoid the occurrence of ln(0) in the calculations. This step might introduce bias in the ApEn, which introduces two downsides in practice: First, ApEn is heavily dependent on the record length and is uniformly lower than expected for short records. Second, the ApEn analysis sometimes lacks relative consistency. That is, if the ApEn of one dataset is lower than that of another, it does not remain lower for all conditions tested, even though it should. Particularly, in the vicinity of low order resonances, although TBT readings are regular due to a low periodicity, such motions are vulnerable to errors. Therefore, it might be better to use ApEn along with other chaos maps, such as FMA, to identify the chaos from different aspects in the nonlinear beam dynamics. All these chaos maps share the same times series (TBT data) and can be implemented in parallel.

Thus far, only an electron ring lattice dedicated as a synchrotron light source has been tested. Applying ApEn to other types of circular accelerators, such as hadron colliders, is worth further exploration. Besides ApEn, many other entropy algorithms, such as Kolmogorov-Sinai entropy [30,31], sample entropy [18], Fuzzy entropy [32], etc., are also available for analyzing nonlinear systems. Each algorithm has its pros and cons in quantifying chaos. Some further exploration of applying entropy analysis to beam dynamics might be interesting.

ACKNOWLEDGMENTS

This research used resources of the National Synchrotron Light Source II, a U.S. Department of Energy (DOE) Office of Science User Facility operated for the DOE Office of Science by Brookhaven National Laboratory under Contract No. DE-SC0012704.

[1] A. Chao, M. Tigner, H. Weise, and F. Zimmermann, *Handbook of Accelerator Physics and Engineering* (World Scientific, Singapore, 2023), 3rd ed., Chap. 2.3.7, p. 140.

[2] A. Bazzani, M. Giovannozzi, C. E. Montanari, and G. Turchetti, Performance analysis of indicators of chaos for nonlinear dynamical systems, Phys. Rev. E **107**, 064209 (2023).

[3] A. Wolf, J. Swift, H. Swinney, and J. Vastano, Determining lyapunov exponents from a time series, Physica D (Amsterdam) **16**, 285 (1985).

[4] F. Schmidt, F. Zimmermann, and F. Willeke, Comparison of methods to determine long-term stability in proton storage rings, Part. Accel. **35**, 249 (1991).

[5] S. Habib and R. Ryne, Symplectic calculation of Lyapunov exponents, Phys. Rev. Lett. **74**, 70 (1995).

[6] J. Laskar, Introduction to frequency map analysis, in *Hamiltonian Systems with Three or More Degrees of Freedom* (Springer, Dordrecht, 1999), pp. 134–150.

[7] F. Panichi, K. Goździewski, and G. Turchetti, The reversibility error method (REM): A new, dynamical fast indicator for planetary dynamics, Mon. Not. R. Astron. Soc. **468**, 469 (2017).

[8] Y. Li, Y. Hao, K. Hwang, R. Rainer, A. He, and A. Liu, Fast dynamic aperture optimization with forward-reversal integration, Nucl. Instrum. Methods Phys. Res., Sect. A **988**, 164936 (2021).

[9] M. Borland, Elegant: A flexible SDDS-compliant code for accelerator simulation, Argonne National Laboratory, Technical Report Advanced Photon Source Report No. LS-287, 2000.

[10] Y. Li, J. Wan, A. Liu, Y. Jiao, and R. Rainer, Data-driven chaos indicator for nonlinear dynamics and applications on storage ring lattice design, Nucl. Instrum. Methods Phys. Res., Sect. A **1024**, 166060 (2022).

[11] Y. Li, K. Hwang, C. Mitchell, R. Rainer, R. Ryne, and V. Smaluk, Design of double-bend and multibend achromat lattices with large dynamic aperture and approximate invariants, Phys. Rev. Accel. Beams **24**, 124001 (2021).

[12] S. Pincus, Approximate entropy as a measure of system complexity, Proc. Natl. Acad. Sci. U.S.A. **88**, 2297 (1991).

[13] S. Pincus and R. Kalman, Irregularity, volatility, risk, and financial market time series, Proc. Natl. Acad. Sci. U.S.A. **101**, 13709 (2004).

[14] C. Volos, S. Jafari, J. Munoz-Pacheco, J. Kengne, and K. Rajagopal, Nonlinear dynamics and entropy of complex systems with hidden and self-excited attractors II, Entropy **22**, 1428 (2020).

[15] X. Huang, Robust simplex algorithm for online optimization, Phys. Rev. Accel. Beams **21**, 104601 (2018).

[16] S. Pincus, Approximate entropy (ApEn) as a complexity measure, Chaos **5**, 110 (1995).

[17] Peter Grassberger and Itamar Procaccia, Measuring the strangeness of strange attractors, Physica D (Amsterdam) **9**, 189 (1983).

[18] J. S. Richman and J. Randall Moorman, Physiological time-series analysis using approximate entropy and sample entropy, Am. J. Physiol. Heart Circ. Physiol. **278**, H2039 (2000).

[19] J. Eckmann and D. Ruelle, Ergodic theory of chaos and strange attractors, Rev. Mod. Phys. **57**, 617 (1985).

[20] G. Manis, Fast computation of approximate entropy, Comput. Methods Programs Biomed. **91**, 48 (2008).

[21] M. Flood and B. Grimm, Entropyhub: An open-source toolkit for entropic time series analysis, PLoS One **16**, e0259448 (2021).

[22] M. Hénon, Numerical study of quadratic area-preserving mappings, Q. Appl. Math. **27**, 291 (1969).

[23] H. Yoshida, Construction of higher order symplectic integrators, Phys. Lett. A **150**, 262 (1990).

[24] D. Robin, C. Steier, J. Laskar, and L. Nadolski, Global dynamics of the advanced light source revealed through experimental frequency map analysis, Phys. Rev. Lett. **85**, 558 (2000).

[25] K. Deb, A. Pratap, S. Agarwal, and T. Meyarivan, A fast and elitist multiobjective genetic algorithm: NSGA-II, IEEE Trans. Evol. Comput. **6**, 182 (2002).

[26] L. Yang, Y. Li, W. Guo, and S. Krinsky, Multiobjective optimization of dynamic aperture, Phys. Rev. ST Accel. Beams **14**, 054001 (2011).

[27] Y. Li, W. Cheng, L-H. Yu, and R. Rainer, Genetic algorithm enhanced by machine learning in dynamic aperture optimization, Phys. Rev. Accel. Beams **21**, 054601 (2018).

[28] M. Borland, L. Emery, V. Sajaev, and A. Xiao, Multiobjective optimization of a lattice for potential upgrade of the Advanced Photon Source, in *Proceedings of 24th Particle Accelerator Conference, PAC'11, New York, USA, 2011* (2011), pp. 2354–2356.

[29] C. Bernardini, G. Corazza, G. Di Giugno, G. Ghigo, J. Haissinski, P. Marin, R. Querzoli, and B. Touschek, Lifetime and beam size in a storage ring, Phys. Rev. Lett. **10**, 407 (1963).

[30] A. Shiryayev, New metric invariant of transitive dynamical systems and automorphisms of Lebesgue spaces, *Selected Works of AN Kolmogorov: Volume III: Information Theory and the Theory of Algorithms* (Springer, Dordrecht, 1993), pp. 57–61.

[31] Y. Sinai, Kolmogorov-Sinai entropy, Scholarpedia **4**, 2034 (2009).

[32] A. De Luca and S. Termini, A definition of a nonprobabilistic entropy in the setting of fuzzy sets theory, *Readings in Fuzzy Sets for Intelligent Systems* (Elsevier, New York, 1993), pp. 197–202.